Chemical Science

ROYAL SOCIETY OF CHEMISTRY

EDGE ARTICLE

View Article Online
View Journal | View Issue

Cite this: *Chem. Sci.*, 2025, **16**, 9326

All publication charges for this article have been paid for by the Royal Society of Chemistry

Icosahedron kernel defect in Pt_1Ag_x series of bimetallic nanoclusters enhances photocatalytic hydrogen evolution†

Dong Tan,‡[a] Tengfei Ding,‡[a] Kaidong Shen,‡[a] Chang Xu,[a] Shan Jin,[b] Daqiao Hu,*[a] Song Sun*[a] and Manzhou Zhu*[a]

Received 5th March 2025
Accepted 8th April 2025

DOI: 10.1039/d5sc01735a

rsc.li/chemical-science

Developing high-efficiency photocatalysts for photocatalytic hydrogen production and understanding the structure–property relationships is much desired. In this study, a family of Pt_1Ag_x (x = 9, 11, 13 and 14) nanoclusters (NCs), including a new $Pt_1Ag_{11}(SR)_5(P(Ph\text{-}OMe)_3)_7$ NC, were designed and synthesized *via* ligand engineering (SR = 2,3,5,6-tetrafluorothiophenol, P(Ph-OMe)$_3$ = tris(4-methylphenyl)phosphine). The positive effect of the kernel structural defect on photocatalytic activity was investigated using the photocatalytic water-splitting reaction as a model, and the mechanistic relationship between the defect structure and catalytic activity was clarified. In this series of Pt_1Ag_x bimetallic NCs, the Pt_1Ag_{11} NC, which exhibits a distinctive defect-containing icosahedral kernel structure, displayed excellent catalytic performance for photocatalytic hydrogen evolution, with the hydrogen production rate reaching 1780 μmol g^{-1} h^{-1}. The experimental results revealed that the superior catalytic activity of Pt_1Ag_{11}/g-C_3N_4 may originate from the formation of Z-scheme heterojunction between Pt_1Ag_{11} and the g-C_3N_4, facilitating efficient electron–hole separation and charge transfer. Furthermore, density-functional theory (DFT) calculations reveal the critical role of the defect-containing icosahedron-kernel on photocatalytic activity, which is favourable for the formation of the most stable nanocomposites and the easy absorption of H* intermediates on the Ag sites in Pt_1Ag_{11}/g-C_3N_4. This paper provides insights into the effect that the defects have on the mechanism of the photocatalytic hydrogen evolution reaction at the atomic level and promotes the rational design of high-efficiency photocatalysts.

1 Introduction

Photocatalytic water splitting for hydrogen production has attracted extensive interest because it offers a pollution-free and sustainable route to alleviate the energy crisis and tackle environmental issues.[1–3] However, achieving high conversion efficiency remains a significant challenge due to the complex processes involved in photocatalytic reactions, including photo absorption, charge separation, transport, dissociation, and recombination.[4,5] Therefore, the development of high-efficiency photocatalysts for photocatalytic hydrogen production, and a detailed understanding of structure–property relationships, are desired.[6]

Atomic scale metal nanoclusters (NCs) (1–3 nm in diameter) have shown potential for application in photocatalysis due to their unique atomic stacking modes, optical properties and abundance of catalytic active sites.[7,8] Moreover, their ultrasmall size endows metal NCs with discrete molecule-like electronic energy levels, whereby they can be excited as small-band-gap semiconductors to generate electrons and holes.[9] To avoid the unfavorable agglomeration of metal NCs caused by high surface energies during the photocatalytic reaction, NC-based composite photocatalysts were fabricated to improve catalytic stability and activity.[10,11] In 2013, Negishi *et al.* reported glutathione-protected Au_{25} NCs loaded onto $BaLa_4Ti_4O_{15}$ as hybrid catalysts for the water-splitting reaction; the hybrid catalysts exhibited photocatalytic activity 2.6 times higher than that of co-catalysts loaded with larger gold nanoparticles (10–30 nm).[12] Subsequently, a wide range of metal NCs has been used in photocatalytic hydrogen evolution.[13] For instance, Lu *et al.* synthesized $Pt_5(GSH)_{10}$ NCs and immobilized them on multi-arm CdS nanorods (NRs). The Pt NCs extracted the photoinduced electrons of the CdS NRs and enhanced charge separation, thereby ensuring the Pt_5–CdS composite catalysts exhibited an improved photocatalytic H_2 production rate of 13.0 mmol g^{-1} h^{-1} H_2.[14] Wang *et al.* synthesized Ag_{44} NCs and

[a]*Department of Chemistry and Centre for Atomic Engineering of Advanced Materials, Key Laboratory of Structure and Functional Regulation of Hybrid Materials of Ministry of Education, Anhui University, Hefei, Anhui 230601, China. E-mail: hudaqiao@ahu.edu.cn; suns@ustc.edu.cn; zmz@ahu.edu.cn*

[b]*Institutes of Physical Science and Information Technology, Anhui University, Hefei, Anhui 230601, China*

† Electronic supplementary information (ESI) available. CCDC 2380779. For ESI and crystallographic data in CIF or other electronic format see DOI: https://doi.org/10.1039/d5sc01735a

‡ D. Tan, T. Ding and K. Shen contributed equally to this work.

immobilized them on TiO_2. The photocatalytic H_2 production of Ag_{44}–TiO_2 was 7.4 mmol g^{-1} h^{-1}. This elevated performance of Ag_{44}–TiO_2 was attributed to both the extension of the photoresponse time and the efficient separation and transport of charge carriers.[15] Several methods have been proposed to utilize photogenerated carriers effectively for photocatalysis, such as heteroatom doping or Z-scheme heterojunctions,[10,16–19] however, the efficient charge transfer and separation of NC-based hybrid catalysts in photocatalytic reactions still poses a challenge.[20]

Previous work has revealed that a NC structure that contains defects can significantly enhance catalytic performance. For example, Nematulloev *et al.* reported that defect-containing Cu_{28} NCs have structural vertex defects which cause a distortion in the framework and lower the symmetry, thus exhibiting more efficient selectivity in C–C cross-coupling reactions compared with Cu_{29} NCs.[21] In addition, Silalahi *et al.* reported the discovery of hydride-containing 2-electron palladium/copper superatomic alloys, namely $PdHCu_{11}$ and $PdHCu_{12}$. The distinctive defects in $PdHCu_{11}$ expose the central Pd atom, thus providing an active site to catalyze the reaction, resulting in better hydrogen evolution reaction activity than $PdHCu_{12}$.[22] A few reports have been published on the structural defects of metal NCs for catalysis; however, the effect of defects on the formation of heterojunctions or related mechanisms for enhanced photocatalysis have not yet been clarified for composite photocatalysts.

Herein, $Pt_1Ag_{11}(SR)_5(P(Ph\text{-}OMe)_3)_7$ (Pt_1Ag_{11} for short, where SR is 2,3,5,6-tetrafluorothiophenol and $P(Ph\text{-}OMe)_3$ is tris(4-methylphenyl)phosphine) with three vertex Ag atom defects within the icosahedral kernel was synthesized to construct NCs that exhibit a defect effect. The X-ray crystal structure of Pt_1Ag_{11} was identified and categorized as belonging to the Pt_1Ag_x family (x = 9, 11, 13 and 14) (Scheme 1). Considering this, the relationship between the defect-containing icosahedral kernel and the catalytic activity was established using photocatalytic water splitting as a model. Nanocomposite photocatalysts were prepared by loading four Pt_1Ag_x NCs onto two-dimensional graphite-like carbon nitride (g-C_3N_4). g-C_3N_4 has a sheet-like structure with a suitable bandgap, is easily functionalized, and exhibits excellent thermal stability, and chemical corrosion resistance.[23,24] In this series of Pt_1Ag_x bimetallic NCs, the Pt_1Ag_{11} NC, which exhibits a distinctive defect-containing icosahedral kernel structure displayed excellent catalytic performance for photocatalytic hydrogen evolution, with the hydrogen production rate reaching 1780 μmol g^{-1} h^{-1}. The superior catalytic activity of Pt_1Ag_{11}/g-C_3N_4 may originate from the formation of a Z-scheme heterojunction between the two materials, facilitating the extension of the photoresponse time whilst facilitating more efficient electron–hole separation and charge transfer. Theoretical calculations further demonstrated that defects within the icosahedral kernel facilitated electron transport and separation. This paper offers a detailed understanding of how defects influence the photocatalytic hydrogen evolution reaction at the atomic level, facilitating the rational design of efficient photocatalysts.

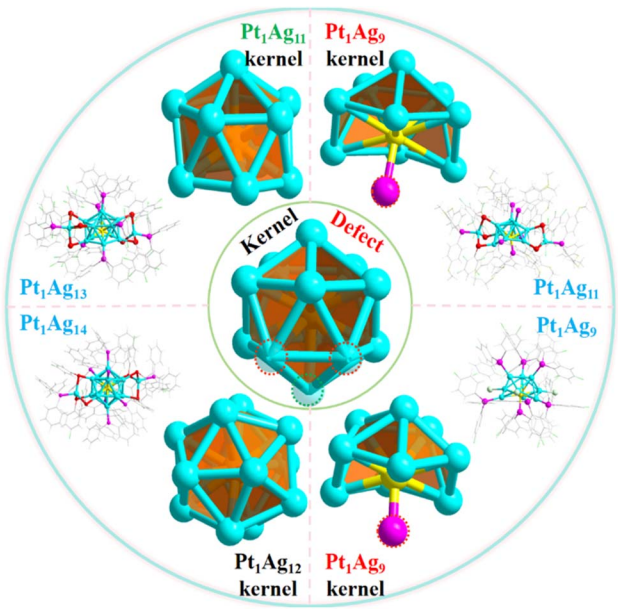

Scheme 1 Structure of the Pt_1Ag_x series of nanoclusters (including the kernel and the whole structure). Color code: Pt-yellow, Ag-turquoise, S-red, P-pink, F-bright green, Cl-green, O-orange, C-grey.

2 Experimental section

2.1 Chemicals

Most reagents were purchased from Sigma-Aldrich and used without further purification, including hexachloroplatinic (IV) acid ($H_2PtCl_6 \cdot 6H_2O$, 99.99%, metals basis), potassium tetrachloroplatinate (K_2PtCl_4, 99.9%, metals basis), silver nitrate ($AgNO_3$), 2,3,5,6-tetrafluorothiophenol (SR, $C_6H_2F_4S$), pentafluorobenzenethiol (PFBT, C_6HF_5S), 2-chloro-4-fluorobenzenethiol (C_6H_4FClS), sodium borohydride ($NaBH_4$), tris(4-fluorophenyl) phosphine ($P(Ph\text{-}F)_3$), tris(4-methylphenyl)phosphine ($P(Ph\text{-}OMe)_3$) and triphenylphosphine (PPh_3). 5,5-Dimethyl-1-pyrroline-1-oxide (DMPO), tetraphenyl phosphonium bromide (PPh_4Br, 98%), methylene chloride (CH_2Cl_2, HPLC), methanol (CH_3OH, HPLC) and *n*-hexane (HeX, HPLC grade) were purchased from Energy Chemical.

2.2 Synthesis of $Pt_1Ag_{11}(SR)_5(P(Ph\text{-}OMe)_3)_7$

40 mg of $AgNO_3$ and $H_2PtCl_6 \cdot 6H_2O$ (12 mg, 0.0225 mmol) were dissolved into 10 mL of methanol in a 50 mL round-bottomed flask. The solution was stirred vigorously at room temperature for 10 min. The solution immediately turned brown. Subsequently, 40 μL of 2,3,5,6-tetrafluorothiophenol was added into the flask. After 5 min of reaction, 200 mg of tris(4-methylphenyl) phosphine dissolved in 10 mL of CH_2Cl_2 was added under vigorous stirring. The color of the solution became transparent. After half an hour, 3 mL of an aqueous solution of $NaBH_4$ (80 mg) was added quickly to the reaction mixture under vigorous stirring. The solution color immediately changed from brown to black. The reaction was subsequently carried out for a duration of 9 hours under a N_2 atmosphere at room temperature. The

crystals were crystallized from CH_2Cl_2/hexane at room temperature in the dark to afford red block single crystals after 2 weeks.

2.3 Synthesis of $Pt_1Ag_{14}(SR)_6(P(Ph\text{-}F)_3)_8$

40 mg of $AgNO_3$ and $H_2PtCl_6 \cdot 6H_2O$ (12 mg, 0.0225 mmol) were dissolved into 10 mL of methanol in a 50 mL round-bottomed flask. The solution was stirred vigorously at room temperature for 10 min. The solution immediately turned brown. Subsequently, 40 μL of 2,3,5,6-tetrafluorothiophenol was added into the flask. After 5 min of reaction, 200 mg of tris(4-fluorophenyl) phosphine dissolved in 10 mL of CH_2Cl_2 was added under vigorous stirring. The color of the solution became transparent. After half an hour, 2 mL of an aqueous solution of $NaBH_4$ (25 mg) was added quickly to the reaction mixture under vigorous stirring. The solution color immediately changed from brown to black. The reaction was subsequently carried out for a duration of 22 h under a N_2 atmosphere at room temperature. The crystals were crystallized from CH_2Cl_2/hexane at room temperature in the dark to afford orange-red block single crystals after 5 days.

2.4 Synthesis of $Pt_1Ag_{14}(SR)_6(PPh_3)_8$

40 mg of $AgNO_3$ and $H_2PtCl_6 \cdot 6H_2O$ (12 mg, 0.0225 mmol) were dissolved into 10 mL of methanol in a 50 mL round-bottomed flask. The solution was stirred vigorously at room temperature for 10 min. The solution immediately turned brown. Subsequently, 40 μL of 2,3,5,6-tetrafluorothiophenol were added into the flask. After 5 min of reaction, 200 mg of triphenylphosphine dissolved in 10 mL of CH_2Cl_2 was added under vigorous stirring. The color of the solution became transparent. After half an hour, 2 mL of an aqueous solution of $NaBH_4$ (40 mg) was added quickly to the reaction mixture under vigorous stirring. The solution color immediately changed from brown to black. The reaction was subsequently carried out for a duration of 12 h under a N_2 atmosphere at room temperature. The crystals were crystallized from CH_2Cl_2/hexane at room temperature in the dark to afford yellow rod-like single crystals after 2 weeks.

2.5 Synthesis of the g-C_3N_4 nanosheet

Pristine g-C_3N_4 was synthesized *via* a thermal polymerization method. 5 g of melamine was calcined at 550 °C for 4 h at a rate of 5 °C min^{-1} in a muffle furnace. Then, the resulting yellow sample was collected and spread in a crucible, then calcined at 500 °C for 2 h at a heating rate of 5 °C min^{-1} to obtain the carbon nitride nanosheet.

2.6 Preparation of Pt_1Ag_x/g-C_3N_4 nanocomposites

For the preparation process, 5 mg of PtAg nanoclusters were dissolved in 10 mL of methylene chloride in a round-bottom flask (RBF), which gave a medium to intense color. To the brown-colored solution, 100 mg of g-C_3N_4 nanosheet were added and the mixture was stirred for 12 h. The color of the supernatant became faint as the nanoclusters were successfully embedded onto the g-C_3N_4 nanosheet. The reaction mixture was then centrifuged at 8000 rpm for 10 min. The clear DCM layer was discarded, and the g-C_3N_4 precipitate was dried under vacuum for a few hours. The dry powder was characterized *via* TEM analyses and used for the catalytic reactions.

2.7 Characterization

The data collection for the single-crystal X-ray diffraction (SC-XRD) analysis of all the nanocluster crystal samples was carried out on a Stoe Stadivari diffractometer under a nitrogen flow, using graphite-monochromatized Cu Kα radiation (λ = 1.54186 Å). Data reductions and absorption corrections were performed using the SAINT and SADABS programs, respectively. The structure was solved by direct methods and refined with full-matrix least squares on F2 using the SHELXTL software package. All non-hydrogen atoms were refined anisotropically, and all the hydrogen atoms were set in geometrically calculated positions and refined isotropically using a riding model. All crystal structures were treated with PLATON SQUEEZE. The diffuse electron densities from these residual solvent molecules were removed. The CCDC number of Pt_1Ag_{11} is 2380779.

Electrospray ionization mass spectrometry (ESI-MS) measurements were performed on a MicrOTOF-QIII high-resolution mass spectrometer. All UV-vis spectra of the nanoclusters were recorded using an Agilent 8453, and the samples were dissolved in CH_2Cl_2 whose background correction was made using a CH_2Cl_2 blank. Transmission electron microscopy (TEM, JEM-2010) was used to investigate the morphologies and energy-dispersive X-ray spectroscopy (EDS) analyses were performed on a JEOL JEM-2100F FEG TEM operated at 200 kV. Nanocluster powder samples were used for the analysis. X-ray photoelectron spectroscopy (XPS, Thermo-VG Scientific, E = 1486.60 eV, Mg Kα radiation, USA) measurements were performed to detect the elemental composition. The samples were analyzed for photoluminescence spectra using a MicroTime 200 fluorescence spectrophotometer at room temperature. The emission lifetimes were measured with nanoclusters on a HORIBA FluoroMax-4P. The nanocluster was purged with N_2 for 5 min, then saturated with O_2 for 5 min, respectively.

The powder X-ray diffraction (PXRD) measurements of the materials were carried out using a diffractometer operating (Smartlab 9 kW, Cu Kα radiation) at 40 kV and 200 mA, in a 2θ range of 10–80° with a step width of 0.01°. Fourier-transform infrared spectroscopy (FT-IR) was collected on a Thermo Scientific Nicolet iS50R spectrometer. UV-vis diffuse reflectance spectroscopy (DRS) was conducted on a Shimadzu UV-2600i spectrophotometer at room temperature using $BaSO_4$ as the reference. The electron paramagnetic resonance (EPR) spectra were obtained using a JEOL JES FA200 to detect $^{\bullet}O_2^-$ and $^{\bullet}OH$ radicals using 5,5-dimethyl-1-pyrroline-1-oxide (DMPO) as a spin trap. Inductively coupled plasma-atomic emission spectrometry (ICP-AES) measurements were performed on an Atomscan advantage instrument from Thermo Jarrell Ash Corporation (USA), whereby 2.5 mg of PtAg NC/g-C_3N_4 nanocomposites were dissolved in 1 mL of concentrated nitric acid and 3 mL of deionized water for testing.

2.8 Photoelectrochemical measurements

The electrochemical impedance spectroscopy (EIS), photocurrent–time profiles and Mott–Schottky diagram were recorded on a CHI760E electrochemical workstation with a standard three-electrode system, where photocatalyst-coated fluorine-doped tin oxide (FTO) was used as the working electrode, Pt plate as the counter electrode, and a saturated Ag/AgCl electrode as the reference electrode. A 0.1 M Na_2SO_4 solution was used as the electrolyte. The as-synthesized samples (10 mg) were added into 400 μL of ethanol and a 20 μL Nafion mixed solution, and the working electrodes were prepared by dropping the suspension (200 μL) onto an FTO glass substrate before drying at room temperature. Mott–Schottky plots were measured at 500, 1000, and 1500 Hz, respectively. EIS was recorded with a bias potential of −1.4 V in the dark.

2.9 Photocatalytic hydrogen evolution

The photocatalytic hydrogen production tests were performed in a Pyrex top-irradiation reaction vessel with a stationary temperature at 25 °C under full-spectrum light, which was connected to a glass closed gas system (Labsolar-6A, Perfect Light). A 300 W Xe lamp was employed to serve as the light source. 50 mg of the as-prepared photocatalyst was ultrasonically dissolved in 10 mL of triethanolamine (TEOA, sacrifice reagent) and 90 mL of H_2O and then loaded into a 370 mL sealed quartz reactor and evacuated using a vacuum pump. The photocatalytic hydrogen performance of the photocatalyst was calculated using gas chromatography (GC-5190, China) equipped with a thermal-conductivity detector (TCD, with Ar as the carrier gas and a 5 Å molecular sieve column). The injection temperature and detection temperature were set to 100 °C during testing, and the column furnace temperature was set to 50 °C. The production of H_2 every 30 min was monitored using a gas chromatograph. The temperature of the whole process was kept at 8 °C using circulating cooling water.

2.10 Apparent quantum efficiency (AQE) measurements

The AQE measurement methods were similar with those of the photocatalytic measurements except for the wavelength of the light. Particularly, different monochromatic light (360 nm, 380 nm, 400 nm, 420 nm, 440 nm) was utilized to assess the quantum efficiency of the photocatalyst. Based on the amounts of evolved H_2, the AQE is calculated *via* the following formula:

$$\begin{aligned}\mathrm{AQE} &= \frac{\text{the number of reacted electrons}}{\text{the number of incident photons}} \times 100\% \\ &= \frac{N_e}{N_p} \times 100\% \\ &= \frac{(2 \times v) \times N_A}{E_{total}/E_{photon}} \times 100\% \\ &= \frac{(2 \times v) \times N_A \times \hbar \times c}{S \times P \times \lambda} \times 100\% \\ &= \frac{(2 \times v) \times N_A \times \hbar \times c}{S \times P \times \lambda} \times 100\%\end{aligned}$$

where n (mol) refers to the amount of H_2 molecules, v (mol s^{-1}) represents the rate of H_2 production, N_A (6.022×10^{23} per mol) represents the Avogadro constant, $\hbar$ (6.626×10^{-34} J S) represents the Planck constant, c (3×10^8 m s^{-1}) is the speed of light, S is the irradiation area (cm^2), P refers the intensity of the irradiation light (W cm^{-2}), t signals the photoreaction time (s), and λ is the wavelength of the monochromatic light (m).

The simplified formula is translated as follows:

$$\mathrm{AQE} = \frac{0.2394 \times v}{S \times P \times \lambda} \times 100\%$$

2.11 Computational method

The Vienna *ab initio* simulation package (VASP) was selected to perform our density-functional theory (DFT) calculations. The exchange–correlation functional was treated through the generalized gradient approximation (GGA) using the Perdew–Burke–Ernzerhof (PBE) functional. The cutoff energy was set to 570 eV for all calculations. The Brillouin zone (BZ) was sampled using a 2 × 2 × 1 gamma-centered Monkhorst–Pack grid. The energy and the force standard received on each atom were set to be 10^{-6} eV and 0.02 eV $Å^{-1}$, respectively. To avoid the interaction between adjacent slabs, a vacuum space of 20 Å was used. The visualization for electronic and structural analysis software (VESTA 3) was utilized for visualization and plotting. The VASPKIT code was employed for the postprocessing of the calculated data.

The charge density difference ($\Delta\rho$) was determined by

$$\Delta\rho = \rho_{*M} - \rho_M - \rho_* \quad (1)$$

where ρ_* and ρ_M represent the charge densities of the g-C_3N_4 monolayer and the clusters (Pt_1Ag_9, Pt_1Ag_{11}, Pt_1Ag_{13} or Pt_1Ag_{14}) and ρ_{*M} refers to total charge densities of the cluster-adsorbed g-C_3N_4 systems.

In addition, Bader charges were utilized to detect charge transfer between the substrate and clusters. To evaluate the energetic stability of the g-C_3N_4-loaded clusters, we calculated their binding energy (E_{bind}), which is defined as:

$$E_{bind} = E_{*M} - E_* - E_M \quad (2)$$

where E_{*M}, E_* and E_M are the total energies of the M-adsorbed g-C_3N_4 monolayer, pure g-C_3N_4 monolayer and the clusters M (Pt_1Ag_9, Pt_1Ag_{11}, Pt_1Ag_{13} and Pt_1Ag_{14}), respectively. The value of E_{bind} reflects the interaction between the anchored species and the catalyst, and a more negative value indicates a stronger interaction. The free energy difference (ΔG) of the HER process was calculated according to the approach proposed by Norskov *et al.* The formula can be defined as below:

$$\Delta G = \Delta E + \Delta E_{zpe} - T\Delta S \quad (3)$$

where ΔE is the adsorption energy, ΔE_{zpe} and ΔS are the difference in the zero-point energy and entropy between the adsorbed state and the gas phase, respectively. Here, $T = 298.15$ K.

The HER can be decomposed into two steps, and the reaction equation can be written as:

$$* + H^+ + e^- \rightarrow H^* \quad (4)$$

$$H^* + H^+ + e^- \rightarrow * + H_2 \quad (5)$$

where * means the adsorbed materials, and H* represent the adsorbed intermediates. For each step of the hydrogen reactions, the free energy difference can be written as:

$$\Delta G_1 = G_{H^*} - \frac{1}{2}G_{H_2} - G_* \quad (6)$$

$$\Delta G_2 = G_* + \frac{1}{2}G_{H_2} - G_{H^*} \quad (7)$$

where ΔG_1 and ΔG_2 denote the free Gibbes energy difference of the proton adsorption and H_2 desorption steps, respectively.

3 Results and discussion

The icosahedral kernel structure was chosen as the model for investigating the defect effect because it is the most widely observed structure in NCs. A novel Pt_1Ag_{11} NC was synthesized, and can be categorized as part of the Pt_1Ag_x NC series along with three previously reported NCs, Pt_1Ag_9,[25] Pt_1Ag_{13} [7] and Pt_1Ag_{14}.[26] Single-crystal X-ray crystallography (SC-XRD) revealed that Pt_1Ag_{11} crystalized in the triclinic space group $P\bar{1}$. The Pt_1Ag_{11} NC comprised a Pt_1Ag_9 kernel, stabilized by five $P(Ph\text{-}OMe)_3$ ligands, one $Ag(SR)_2[P(Ph\text{-}OMe)_3]$ motif and one $Ag(SR)_3[P(Ph\text{-}OMe)_3]$ motif (Fig. 1a). The chemical composition of Pt_1Ag_{11} was definitively confirmed using electrospray ionization mass spectrometry (ESI-MS) in positive ion mode, as shown in the Fig. 1b. The spectrum contained two intense peaks at m/z of 2500.726 Da (calculated = 2500.765 Da) and 2511.792 Da (calculated = 2511.755 Da), corresponding to the characteristic peaks of $Pt_1Ag_{11}(C_6HF_4S)_5(C_{21}H_{21}O_3P)_7Ag_2(CH_3OH)$ and $Pt_1Ag_{11}(C_6HF_4S)_5(C_{21}H_{21}O_3P)_7Ag_2(CH_3ONa)$. Transmission electron microscopy (TEM) images indicated that Pt_1Ag_{11} has a uniform appearance, with an average size of 1.32 nm (Fig. S1†). The UV-vis spectrum of Pt_1Ag_{11} in CH_2Cl_2 displays one strong peak centered at 372 nm and three weak shoulder peaks at 425, 455, and 550 nm (Fig. 1c). For comparison, the UV-vis spectra of the Pt_1Ag_9, Pt_1Ag_{13}, and Pt_1Ag_{14} NCs revealed different absorption peaks (Fig. S2†). Moreover, the Pt_1Ag_x series in the solid state emitted between 600 and 700 nm (Fig. S3†).

A cycle between enhanced emission intensity with N_2 and quenched emission intensity with O_2 was detected for the Pt_1Ag_{11} NC. Meanwhile, the average PL lifetime of the Pt_1Ag_{11} NC was 4.28 μs, which was prolonged to 5.91 μs in a N_2 atmosphere, and reduced to 2.16 μs in an O_2 atmosphere. Similar results were observed for the other three NCs, indicating that the Pt_1Ag_x series of NCs (x = 9, 11, 13, and 14) were phosphorescent[7] (Fig. S4–S6†). In addition, the valence states of the Pt and Ag atoms in the Pt_1Ag_x series of bimetallic NCs were investigated and compared with the results obtained from X-ray photoelectron spectroscopy (XPS). The XPS results revealed the presence of Pt, Ag, P, F, O, C, and S in the Pt_1Ag_{11} NC (Fig. S7†). As shown in Fig. 1d, the Pt 4f binding energies in Pt_1Ag_x were as follows: Pt_1Ag_{14} (71.5 eV) > Pt_1Ag_9 (71.4 eV) > Pt_1Ag_{13} (71.3 eV) > Pt_1Ag_{11} (71.1 eV). The lower binding energies of the Pt 4f peaks indicate that the Pt atoms in Pt_1Ag_{11} were more partial to 0 valence (71.0 eV) compared with the other members of the Pt_1Ag_x family of NCs. For the binding energies of Ag, a sequence of Pt_1Ag_{13} (368.4 eV) ≈ Pt_1Ag_{11} (368.4 eV) > Pt_1Ag_{14} (368.2 eV) ≈ Pt_1Ag_9 (368.2 eV) can be established. This illustrates that the valence state of Ag in the Pt_1Ag_x NCs lies between 0 and +1 (Fig. 1e).

In addition to determining the difference in the electronic structure of the Pt_1Ag_x series of NCs, analysis of their geometric structures is crucial. SC-XRD revealed that Pt_1Ag_{13} crystalized in the triclinic space group $P\bar{1}$ similar to Pt_1Ag_{11}, whereas Pt_1Ag_{14} crystalized in the monoclinic space group $C2/c$; Pt_1Ag_9 was found to have the trigonal space group $R3$ (Tables S1 and S2†).

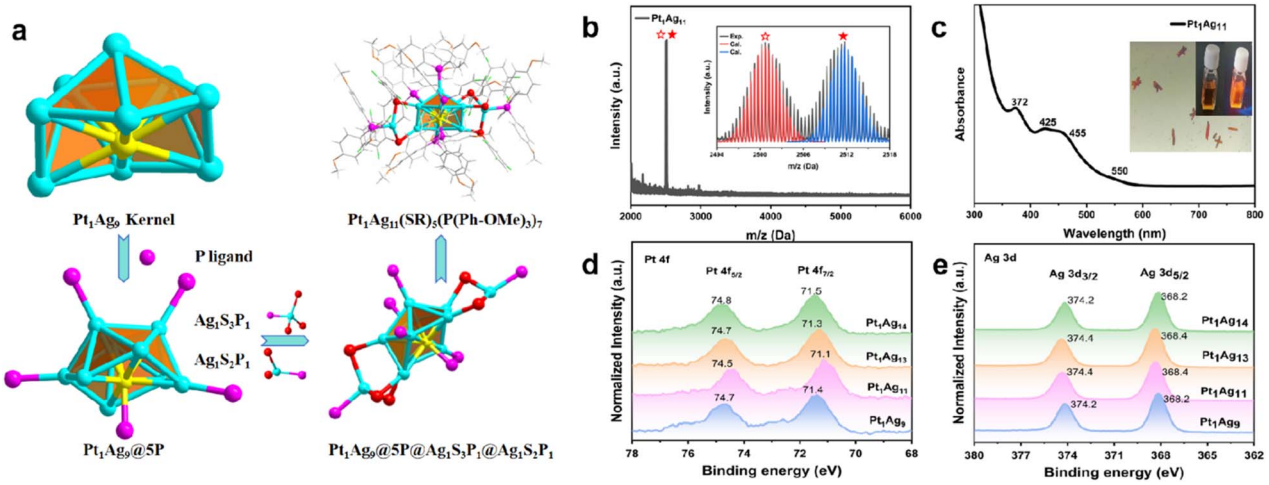

Fig. 1 (a) Structural anatomy of a Pt_1Ag_{11} nanocluster (Pt_1Ag_9 kernel; Pt_1Ag_9@5P; Pt_1Ag_9@$Ag_1S_3P_1$@$Ag_1S_2P_1$; $Pt_1Ag_{11}(C_6H_2F_4S)_5(C_{21}H_{21}O_3P)_7$ overall structure), color labels: yellow, Pt; turquoise, Ag; red, S; pink, P; bright green, F; orange, O; gray, C; white, H. (b) ESI-MS of the Pt_1Ag_{11} nanoclusters [$Pt_1Ag_{11}(C_6HF_4S)_5(C_{21}H_{21}O_3P)_7Ag_2(CH_3OH)$ (☆) and $Pt_1Ag_{11}(C_6HF_4S)_5(C_{21}H_{21}O_3P)_7Ag_2(CH_3ONa)$ (★)]; (c) UV-vis spectra of the Pt_1Ag_{11} nanoclusters. The XPS spectra of (d) Pt 4f and (e) Ag 3d for the Pt_1Ag_x nanoclusters (x = 9, 11, 13, 14).

Comparison of the crystal structures of the Pt_1Ag_x series of NCs indicated that Pt_1Ag_{14} has a complete icosahedral Pt_1Ag_{12} kernel, while the remaining three NCs exhibit different icosahedral-kernel defects (Fig. S8†). In Pt_1Ag_{13}, removing the vertex silver atom from the icosahedral kernel caused the loss of one Ag–P bond, whereas the peripheral $Ag_1S_3P_1$ motif did not change. However, three silver atoms were absent from the icosahedral kernel in Pt_1Ag_{11}, and thus, the $Ag_1S_3P_1$ motif experienced the loss of an Ag–S bond, leading to the formation of the $Ag_1S_2P_1$ motif (Fig. 2a). Meanwhile, a new Pt–P bond was formed within the icosahedral kernels in both Pt_1Ag_{11} and Pt_1Ag_9. Pt_1Ag_{11} and Pt_1Ag_9 have the same kernel, albeit with only a P ligand included for the latter (Fig. 2b). A detailed comparison of the bond lengths and angles within the kernel structures of the Pt_1Ag_9 and Pt_1Ag_{11} NCs further suggested that the kernel of Pt_1Ag_{11} was more distorted (Tables S3 and S4†). In addition, the geometric structures were further compared by analyzing the bond lengths of the four Pt_1Ag_x NCs. The Pt–Ag average distance within the icosahedral kernel in the Pt_1Ag_x NCs was Pt_1Ag_{14} (2.757 Å) > Pt_1Ag_9 (2.747 Å) > Pt_1Ag_{13} (2.744 Å) > Pt_1Ag_{11} (2.743 Å). The Ag–Ag average distance in Pt_1Ag_x was Pt_1Ag_{14} (2.899 Å) > Pt_1Ag_9 (2.891 Å) > Pt_1Ag_{13} (2.873 Å) > Pt_1Ag_{11} (2.861 Å). The above results also indicated that the kernel of the NCs became more compact with the loss of kernel silver atoms. Moreover, the kernel of Pt_1Ag_{11} was the most compact (Fig. S9–S11†). The geometric defects in the icosahedral kernel of the Pt_1Ag_x NCs were correlated with distinct electronic structures. Specifically, both Pt_1Ag_9 and Pt_1Ag_{11} exhibited a free electron count of 6e, while Pt_1Ag_{13} and Pt_1Ag_{14} displayed counts of 7e and 8e, respectively.

The photocatalytic hydrogen evolution reaction was then used to examine the effect of the structural defects on the catalytic activity. A schematic diagram of the photocatalyst preparation process is shown in Scheme S1.†[27] Lamellar g-C_3N_4 nanosheet was first synthesized *via* secondary calcination and exhibited a larger specific surface area (63.9405 $m^2\ g^{-1}$) compared with bulk g-C_3N_4 (10.053 $m^2\ g^{-1}$), as confirmed by BET measurements (Fig. S12†).[28–32] Next, the Pt_1Ag_x NCs with an optimal loading of 5 wt% were anchored onto the g-C_3N_4 nanosheet *via* impregnation (Fig. S13†). Four types of Pt_1Ag_x/g-C_3N_4 nanocomposites labeled Pt_1Ag_9/g-C_3N_4, Pt_1Ag_{11}/g-C_3N_4, Pt_1Ag_{13}/g-C_3N_4, and Pt_1Ag_{14}/g-C_3N_4 were prepared using this method. Inductively coupled plasma-atomic emission spectroscopy (ICP-AES) was utilized for further analysis, unambiguously identifying the similar Pt and Ag contents of the four types of Pt_1Ag_x/g-C_3N_4 nanocomposite (Table S5†). Moreover, TEM images and energy-dispersive X-ray spectroscopy (EDX) elemental mapping confirmed the presence and homogeneous distribution of the Pt_1Ag_x NCs on the g-C_3N_4 nanosheet (Fig. S14†). The Pt_1Ag_x/g-C_3N_4 nanocomposites were further analyzed using X-ray diffraction (XRD). As shown in Fig. S15a,† the two diffraction peaks at 13.0° and 27.7° that correspond to the (100) and (002) diffraction of the typical graphitic interlayer stacking structure of the pure g-C_3N_4 nanosheet did not change in the nanocomposites. Moreover, as shown in Fig. S15b,† the characteristic Fourier-transform infrared (FTIR) peaks located at approximately 810 cm^{-1}, 1200–1650 cm^{-1}, and 3000–3400 cm^{-1}, corresponding to the vibrations of the *s*-triazine ring unit, C–N heterocycles, and amino groups (N–H), respectively, remained unchanged in the NCs compared with those of pure g-C_3N_4 nanosheet. These results indicate that the basic backbone of the g-C_3N_4 nanosheet was still well-maintained after the addition of the Pt_1Ag_x NCs. As shown in Fig. S15c,† the optical absorption intensity of Pt_1Ag_x/g-C_3N_4 was enhanced in the full spectrum compared with that of the pure g-C_3N_4 nanosheet. Moreover, according to the Kubelka–Munk function, the corresponding intrinsic bandgap of the g-C_3N_4 nanosheet, Pt_1Ag_{14}/g-C_3N_4, Pt_1Ag_{13}/g-C_3N_4, Pt_1Ag_9/g-C_3N_4, and Pt_1Ag_{11}/g-C_3N_4 were

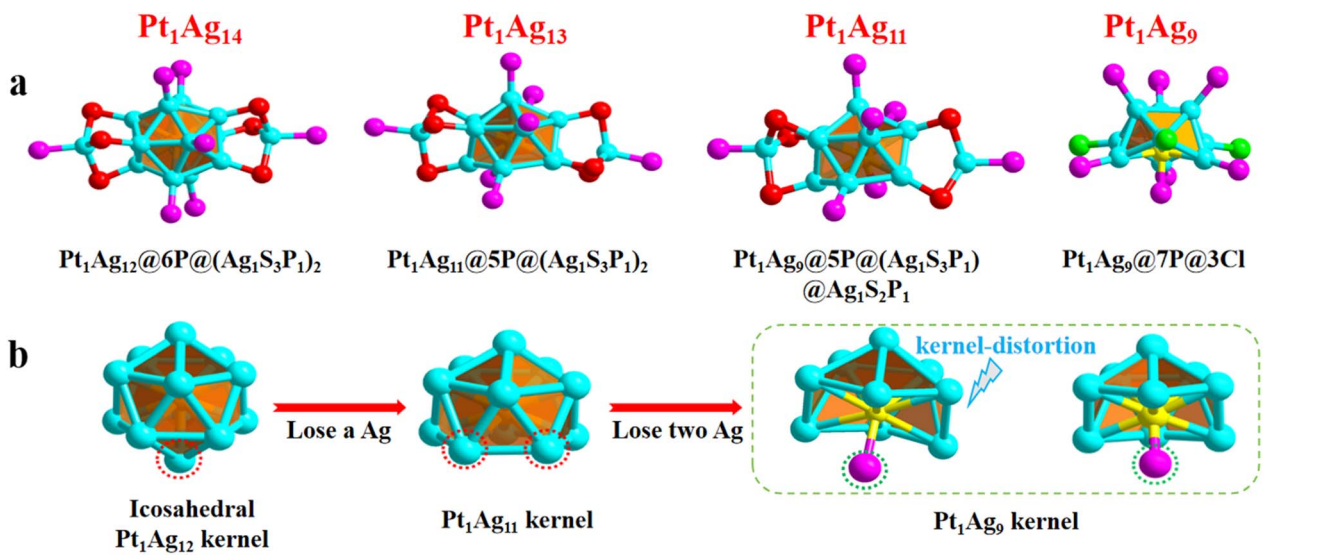

Fig. 2 Structures of the Pt_1Ag_x nanoclusters (x = 9, 11, 13, 14). (a) Framework structure: metallic kernel, ligand, and surface motifs; (b) metallic kernel on the Pt_1Ag_x NCs. Color labels: yellow, Pt; turquoise, Ag; red, S; pink, P; green, Cl. All of the C and H atoms are omitted. The crystal data sources for Pt_1Ag_9, Pt_1Ag_{13} and Pt_1Ag_{14} were taken from the literature.[7,25,26]

estimated to be 2.76, 2.75, 2.73, 2.71 and 2.69 eV, respectively (Fig. S15d†). The enhanced optical absorption intensity and narrowed bandgap of the as-prepared Pt_1Ag_{11}/g-C_3N_4 contributes to the generation of more photogenerated carriers. The hydrogen evolution performance of the four types of Pt_1Ag_x/g-C_3N_4 ($x = 9$, 11, 13, and 14) nanocomposites were then obtained from the full solar spectrum.

As shown in Fig. 3a, when 10 wt% triethanolamine (TEOA) was used as the sacrificial agent, Pt_1Ag_{11}/g-C_3N_4 displayed the highest hydrogen production performance (1780 μmol g^{-1} h^{-1}), which was 33.3 times that of the pure g-C_3N_4 nanosheet (53.4 μmol g^{-1} h^{-1}) and 27.9 times that of Pt_1Ag_{11} (63.8 μmol g^{-1} h^{-1}), as well as outperforming several other corresponding counterparts (Table S6†). To exclude the reaction of the NCs with the sacrificial agent, we performed a set of light–dark contrast tests, which indicated that no hydrogen was produced in the absence of light (Fig. S16†). Moreover, the hydrogen production rate of Pt_1Ag_{11}/g-C_3N_4 was ~2.83 times higher than that of Pt_1Ag_9/g-C_3N_4 (628.4 μmol g^{-1} h^{-1}) and much higher than that of Pt_1Ag_{13}/g-C_3N_4 (448 μmol g^{-1} h^{-1}) and Pt_1Ag_{14}/g-C_3N_4 (185.2 μmol g^{-1} h^{-1}) (Fig. 3b and Table S7†), resulting in the following activity trend; Pt_1Ag_{11}/g-C_3N_4 > Pt_1Ag_9/g-C_3N_4 > Pt_1Ag_{13}/g-C_3N_4 > Pt_1Ag_{14}/g-C_3N_4 > g-C_3N_4 nanosheet. The apparent quantum efficiency of Pt_1Ag_{11}/g-C_3N_4 under light irradiation at 420 nm was ~3.11% (Table S8†). In cycling experiments (Fig. 3c), the hydrogen production rate of Pt_1Ag_{11}/g-C_3N_4 was maintained for three photocatalytic cycles of 9 h. In the fourth cycle, a slight decrease was observed, which may be attributed to shedding of the NCs owing to constant agitation during the cycle reaction. To accurately characterize the changes in the catalysts before and after the reaction, UV-vis diffuse reflection spectroscopy was performed and the characteristic peak position did not change and the intensity decreased slightly, indicating that the overall structure of the catalyst remained unchanged and the structure of Pt_1Ag_{11} was well maintained (Fig. S17†). In addition, the effect of the ligand on the photocatalytic performance was excluded by obtaining the time-dependent H_2 production profiles for various Pt_1Ag_{14} NCs with different ligands (Fig. S18†). As shown in Fig. S19,† the photocatalytic hydrogen production rates of Pt_1Ag_{14}-1/g-C_3N_4, Pt_1Ag_{14}-2/g-C_3N_4, and Pt_1Ag_{14}/g-C_3N_4 were 129.7, 149.8, and 185.2 μmol g^{-1} h^{-1}, respectively. These findings indicated that the influence of the ligand on the photocatalytic performance was minimal.[33]

To better understand the superior photocatalytic hydrogen evolution performance of the Pt_1Ag_{11}/g-C_3N_4 catalysts, a series of photo-electrochemistry tests were performed to probe the electron–hole separation and electron transfer behavior of the nanocomposite photocatalyst.[34–39] As shown in Fig. 3d, Pt_1Ag_{11}/g-C_3N_4 exhibited the strongest transient photocurrent response and the response displayed the following trend under light irradiation, Pt_1Ag_{11}/g-C_3N_4 > Pt_1Ag_9/g-C_3N_4 > Pt_1Ag_{13}/g-C_3N_4 > Pt_1Ag_{14}/g-C_3N_4 > g-C_3N_4 nanosheet, suggesting the promoted efficient separation of the electron–hole pairs in the nanocomposite photocatalysts. This was further confirmed by electrochemical impedance spectroscopy (EIS). The Nyquist curve shown in Fig. 3e indicated that the interfacial charge transfer resistance of Pt_1Ag_{11}/g-C_3N_4 was much smaller than those of g-C_3N_4 and the other Pt_1Ag_x/g-C_3N_4 (x = 9, 13, and 14) nanocomposites. Moreover, steady-state photoluminescence (PL) spectra obtained *via* excitation at 373 nm revealed a broadband centered at 450 nm for the g-C_3N_4 nanosheet and Pt_1Ag_x/g-C_3N_4 nanocomposites with significantly different PL intensities, indicating that the recombination of photogenerated carriers in Pt_1Ag_x/g-C_3N_4 can be efficiently restrained (Fig. S20†). In addition, time-resolved PL spectra (Fig. S21†) were obtained and the fitting of the time-resolved PL spectra determined the PL lifetimes to be 2.089 ns (g-C_3N_4 nanosheet), 2.015 ns (Pt_1Ag_{14}/g-

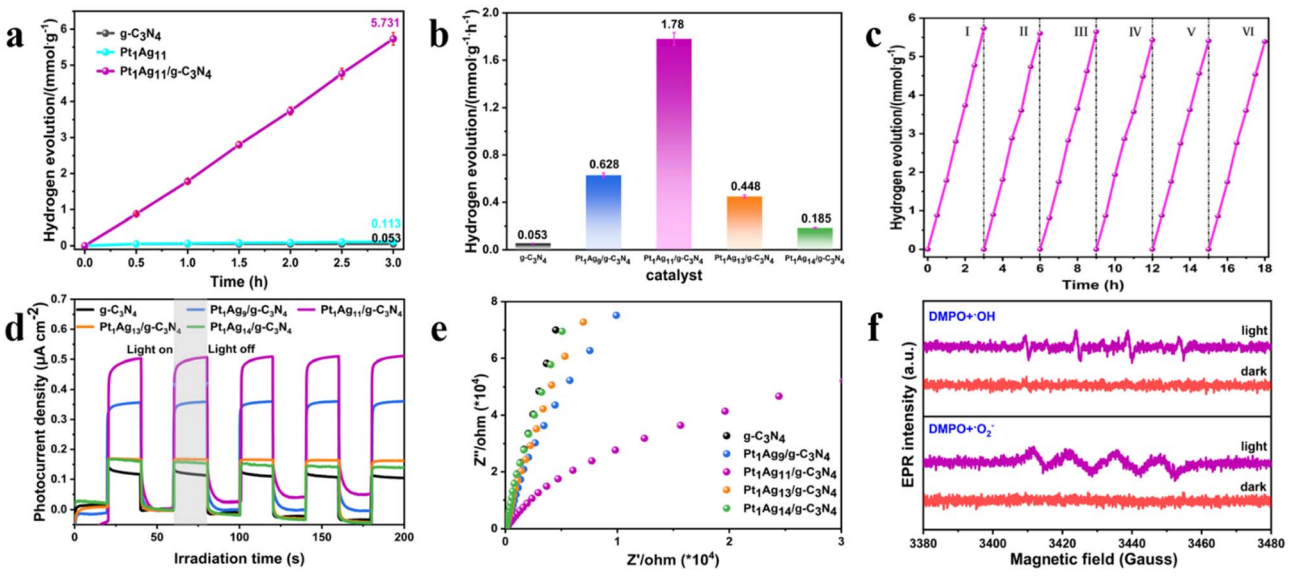

Fig. 3 (a) Photocatalytic H_2 production of Pt_1Ag_{11}, g-C_3N_4 and Pt_1Ag_{11}/g-C_3N_4. (b) Photocatalytic H_2 production of Pt_1Ag_x/g-C_3N_4 (x = 9, 11, 13, and 14). (c) Cycling runs of the Pt_1Ag_{11}/g-C_3N_4 catalyst under light irradiation. (d) Transient photocurrent response and (e) EIS of Pt_1Ag_x/g-C_3N_4 and g-C_3N_4. (f) EPR spectra of $^{\bullet}OH$ and $^{\bullet}O_2^-$ on Pt_1Ag_{11}/g-C_3N_4 under light irradiation or in the dark (x = 9, 11, 13, and 14).

C_3N_4), 1.998 ns (Pt_1Ag_{13}/g-C_3N_4), 1.798 ns (Pt_1Ag_{11}/g-C_3N_4), and 1.619 ns (Pt_1Ag_9/g-C_3N_4). The reduced decay lifetime of Pt_1Ag_x/g-C_3N_4 signified the promotion of efficient separation of electron–hole pairs and an accelerated charge transport process. In summary, the order of charge transfer and separation efficiency of all the photocatalysts closely aligned with the order of the photocatalytic evolution performance.

To understand the photogenerated charge transfer pathways in the Pt_1Ag_x/g-C_3N_4 nanocomposites, the band structure of the g-C_3N_4 nanosheet and Pt_1Ag_x NCs were evaluated. The band gap of 2.76 eV for the g-C_3N_4 nanosheet was determined from the UV-vis absorption spectrum; the conduction band (CB) level was estimated by Mott–Schottky measurements to be −0.31 V *vs.* NHE (PH = 7, Fig. S22†). Because the metal NCs can be regarded as small band gap semiconductors, the energy band structure of the Pt_1Ag_x NCs was determined in the same way as that of the g-C_3N_4 nanosheet (Fig. S23 and S24†).[10,13] The energy diagram showed that all the lowest unoccupied molecular orbitals (LUMO) of the Pt_1Ag_x NCs were slightly more negative than the CB of g-C_3N_4, suggesting the formation of a type-II or Z-scheme heterojunction (Fig. S25†). Taking Pt_1Ag_{11}/g-C_3N_4 as a model, EPR analysis was performed to distinguish the exact types of heterostructures. To produce $^{\bullet}O_2^-$ radicals, the potential of the photogenerated electrons in the CB should be more negative than −0.33 V. Meanwhile, the potential of the photogenerated holes in the valence band (VB) should be more positive than 2.40 V to produce $^{\bullet}OH$ radicals. Apparently, $^{\bullet}O_2^-$ radicals and $^{\bullet}OH$ radicals could not be produced by the type-II heterojunction due to the high potential of the photogenerated electrons of −0.31 V and the low potential of the photogenerated holes of 0.95 V. However, as shown in Fig. 3f, under light irradiation, the production of $^{\bullet}O_2^-$ radicals and $^{\bullet}OH$ radicals was observed, demonstrating the transfer of the photogenerated electrons from g-C_3N_4 to Pt_1Ag_{11}, forming a Z-scheme heterojunction in Pt_1Ag_{11}/g-C_3N_4.[40,41]

To gain a molecular level understanding of the effect of the kernel structural defects on photocatalytic activity, density-functional theory (DFT) calculations using the Vienna *ab initio* simulation package (VASP) were conducted.[42,43] After geometric relaxation, we concluded that the Pt_1Ag_x NCs could maintain a stable structure on the surface of the g-C_3N_4 monolayer (Fig. S26†), which might be attributed to the formation of a Ag–N covalent bond and abundant π–π interactions between Pt_1Ag_x NC and g-C_3N_4. The binding energy (E_{bind}) of the NCs with the g-C_3N_4 monolayer can also be obtained. The E_{bind} value of Pt_1Ag_{11}, Pt_1Ag_9, Pt_1Ag_{13} and Pt_1Ag_{14} were calculated as

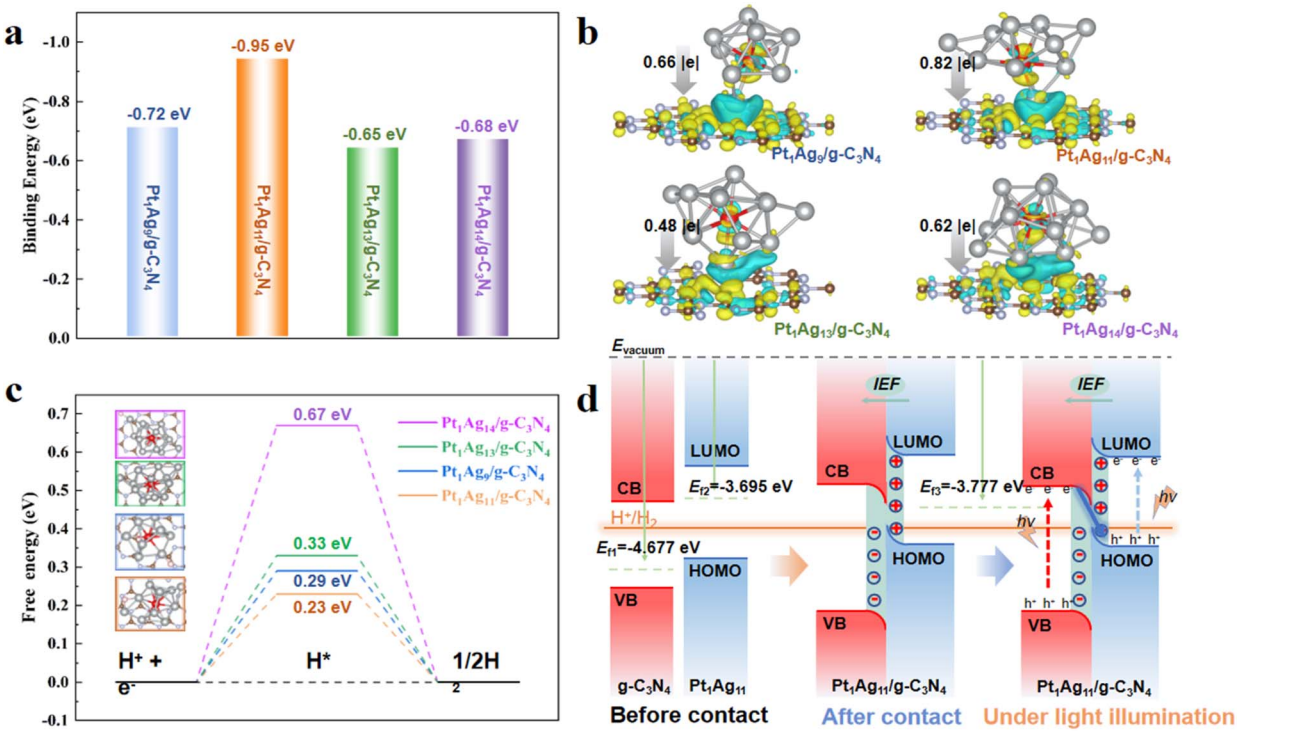

Fig. 4 (a) Binding energies of the Pt_1Ag_x nanoclusters loaded on a g-C_3N_4 monolayer. (b) Differential charge density of nanoclusters loaded on a g-C_3N_4 monolayer, where yellow and cyan areas represent electron accumulation and depletion, respectively. The total amount of charge transfer is given. (c) The calculated Gibbs free energy (ΔG_{H^*}) diagrams for the photocatalytic hydrogen evolution reaction on Pt_1Ag_x/g-C_3N_4. The optimized structures of H* adsorption on Pt_1Ag_9/g-C_3N_4 (blue), Pt_1Ag_{11}/g-C_3N_4 (yellow), Pt_1Ag_{13}/g-C_3N_4 (green), and Pt_1Ag_{14}/g-C_3N_4 (purple). (d) The energy level diagrams and the interface charge transfer route in Pt_1Ag_{11}/g-C_3N_4. An internal electric field (IEF) is formed inside the heterojunction formed by g-C_3N_4 loaded with Pt_1Ag_{11}. E_{vacuum}, E_{f1}, E_{f2} and E_{f3} represent the vacuum level and Fermi levels of g-C_3N_4, Pt_1Ag_{11} and Pt_1Ag_{11}/g-C_3N_4, respectively. VB and CB represent the top of the valence band and the bottom of the conduction band of g-C_3N_4. HOMO and LUMO refer to the highest occupied molecular orbital and the lowest unoccupied molecular orbital of the electrons in the Pt_1Ag_{11} cluster, respectively.

−0.95 eV, −0.72 eV, −0.65 eV and −0.68 eV, respectively, where the high E_{bind} (−0.95 eV) value of Pt_1Ag_{11} enables it to exhibit the most stable loading structure on the g-C_3N_4 surface compared with the other NCs (Fig. 4a). The differential charge density was analyzed to determine the charge transfer between the NCs and monolayers. As shown in Fig. 4b, the g-C_3N_4 layer accumulated negative charge, while the NCs gathered positive charge, thus forming an internal electric field directing from the NCs to g-C_3N_4. Bader[44] charge analysis showed that the Pt_1Ag_9 (0.66|e|) and Pt_1Ag_{11} (0.82|e|) NCs transferred more charge to g-C_3N_4 than was transferred by Pt_1Ag_{13} (0.48|e|) and Pt_1Ag_{14} (0.62|e|). This difference indicates a stronger internal electric field in Pt_1Ag_{11}/g-C_3N_4, allowing Pt_1Ag_{11} to interact more closely with g-C_3N_4. Furthermore, the photocatalytic hydrogen evolution reaction was investigated with ΔG as an indicator of the absorption of H* intermediates on the Ag sites in the Pt_1Ag_x/g-C_3N_4 nanocomposites. As shown in Fig. 4c, Pt_1Ag_{11}/g-C_3N_4 has the lowest Gibbs free energy change (ΔG) (0.23 eV), following the trend of Pt_1Ag_{11}/g-C_3N_4 < Pt_1Ag_9/g-C_3N_4 (0.29 eV) < Pt_1Ag_{13}/g-C_3N_4 (0.33 eV) < Pt_1Ag_{14}/g-C_3N_4 (0.67 eV), which suggests optimal catalytic activity on the surface of the icosahedron with atomic defects. Moreover, the d-band center of the Ag atoms in Pt_1Ag_{11} are closer to the Fermi level, which suggests a stronger binding interaction between Pt_1Ag_{11}/g-C_3N_4 and the H species (Fig. S27†).

Building on this, we explored the mechanism of photocatalytic water splitting for hydrogen production (Fig. 4d). When NCs are loaded onto the surface of g-C_3N_4, free electrons transfer across the interface due to the differing Fermi levels.[45,46] Specifically, electrons from Pt_1Ag_{11}, which has a higher Fermi level, migrate to g-C_3N_4, which has a lower Fermi level, until equilibrium is reached at a common Fermi level. This observation aligns with the differential charge density results shown in Fig. 4b. Under the influence of the Coulomb force, the band edge in g-C_3N_4 at the interface bent downward, and the energy level of Pt_1Ag_{11} bent upward. When illuminated, electrons in the VB of the g-C_3N_4 within the Pt_1Ag_{11}/g-C_3N_4 heterojunctions absorbs the energy and transits it to the CB, leaving behind holes in the VB. Simultaneously, the HOMO electrons of Pt_1Ag_{11} gained energy to transition to the LUMO, resulting in a vacant HOMO. Driven by the internal electric field, the photogenerated electrons in g-C_3N_4 were transferred to Pt_1Ag_{11}. The band (and energy level) bending are crucial for the migration of photogenerated carriers under optical excitation.[47] The downward band bending in g-C_3N_4 facilitates the free flow of electrons while inhibiting hole outflow. Conversely, the upward energy level bending in Pt_1Ag_{11} suppresses electron de-excitation. Thus, electrons flowing from the CB of g-C_3N_4 recombine with the vacant orbitals in the HOMO of Pt_1Ag_{11}, allowing the electrons in the LUMO of Pt_1Ag_{11} to participate in the hydrogen evolution reaction. This process enables direct Z-scheme photocatalytic water splitting for hydrogen production.

4 Conclusions

A family of Pt_1Ag_x (x = 9, 11, 13, and 14) NCs, including the new Pt_1Ag_{11} NC, was designed and synthesized *via* ligand engineering. Single-crystal X-ray diffraction revealed that the crystal structures of these NCs possessed defect-containing icosahedral kernels where one or three vertical Ag atoms are lost. Using the photocatalytic water-splitting reaction as a model, the positive effect of the kernel structural defect on the photocatalytic activity was elucidated, and the mechanism that links the defect structure and catalytic activity was well established. Importantly, Pt_1Ag_{11}/g-C_3N_4 has the highest hydrogen production rate reaching 1780 μmol $g^{-1}\cdot h^{-1}$, that is, ∼2.83, ∼3.97, ∼9.61, and ∼33.3 times higher than that of Pt_1Ag_9/g-C_3N_4, Pt_1Ag_{13}/g-C_3N_4, Pt_1Ag_{14}/g-C_3N_4 and the g-C_3N_4 nanosheets, respectively. DFT calculations further demonstrated the importance of the defect-containing kernel structure for the activation of H_2, electron–hole separation, and the charge transfer efficiency of the Pt_1Ag_{11}/g-C_3N_4 photocatalyst. These improved properties which might be attributed to the formation of Z-scheme heterojunctions, accounting for their very high photocatalytic H_2 production rate. This study lays a strong foundation for the design of highly efficient and precise nanocomposite photocatalysts and provides new insights into the mechanism of photocatalytic hydrogen production at the atomic level.

Abbreviations

Pt_1Ag_{11}	$Pt_1Ag_{11}(SR)_5(P(Ph\text{-}OMe)_3)_7$, (SR is 2,3,5,6-tetrafluorothiophenol and $P(Ph\text{-}OMe)_3$ is tris(4-methylphenyl)-phosphine)
Pt_1Ag_9	$Pt_1Ag_9(P(Ph\text{-}F)_3)_7Cl_3$, ($P(Ph\text{-}F)_3$ is tris(4-fluorophenyl) phosphine)
Pt_1Ag_{13}	$Pt_1Ag_{13}(PFBT)_6(PPh_3)_7$, (PFBT is pentafluorobenzenethiol and PPh_3 is triphenylphosphine)
Pt_1Ag_{14}	$Pt_1Ag_{14}(SR)_6(PPh_3)_8$, (SR is 2-chloro-4-fluorobenzenethiol and PPh_3 is triphenylphosphine)
Pt_1Ag_{14}-1	$Pt_1Ag_{14}(SR)_6(P(Ph\text{-}F)_3)_8$, (SR is 2,3,5,6-tetrafluorothiophenol and $P(Ph\text{-}F)_3$ is tris(4-fluorophenyl)phosphine)
Pt_1Ag_{14}-2	$Pt_1Ag_{14}(SR)_6(PPh_3)_8$, (SR is 2,3,5,6-tetrafluorothiophenol and PPh_3 is triphenylphosphine)

Data availability

CCDC 2380779 contain the supplementary crystallographic data for this paper. These data can be obtained free of charge *via* **https://www.ccdc.cam.ac.uk/data_request/cif**, or by emailing data_request@ccdc.cam.ac.uk, or by contacting The Cambridge Crystallographic Data Centre, 12 Union Road, Cambridge CB2 1EZ, UK; fax: +44 1223 336033.

Author contributions

D. Hu, S. Sun and M. Zhu conceived and designed the project. D. Tan and T. Ding carried out the synthesis and catalytic experiments. S. Jin and D. Tan carried out crystallography and

mass spectrometry. K. Shen and C. Xu conducted theoretical calculations. All authors contributed to the discussion of the results and the preparation of the manuscript.

Conflicts of interest

The authors declare no conflict of interest.

Acknowledgements

We acknowledge the financial support provided by the National Natural Science Foundation of China (22371003, 21871001, 22103001) and the Natural Science Fund of the Education Department of Anhui Province (2023AH050108).

Notes and references

1 Y. Shang, H. Fan, X. Che and W. Wang, Promoted photocatalytic hydrogen evolution via double-electron migration in Ag@g-C_3N_4 heterojunction, *Int. J. Hydrogen Energy*, 2023, **48**, 17370–17382.

2 Y. Han, C. Wang, R. Zhao, J. Han and L. Wang, Ni-doped CdSe/$ZnSnO_3$ double-shell nanocubes heterojunction for efficient photocatalytic hydrogen evolution, *Fuel*, 2023, **353**, 129247.

3 P. Zhou, I. A. Navid, Y. Ma, Y. Xiao, P. Wang, Z. Ye, B. Zhou, K. Sun and Z. Mi, Solar-to-hydrogen efficiency of more than 9% in photocatalytic water splitting, *Nature*, 2023, **613**, 66–70.

4 A. Shu, C. Qin, M. Li, L. Zhao, Z. Shangguan, Z. Shu, X. Yuan, M. Zhu, Y. Wu and H. Wang, Electric effects reinforce charge carrier behaviour for photocatalysis, *Energy Environ. Sci.*, 2024, **17**, 4907.

5 C. Xia, H. Wang, J. K. Kim and J. Wang, Rational Design of Metal Oxide-Based Heterostructure for Efficient Photocatalytic and Photoelectrochemical Systems, *Adv. Funct. Mater.*, 2021, **31**, 2008247.

6 A. Meng, W. Tian, H. Yang, X. Wang, X. Wang and Z. Li, Molybdenum sulfide-modified metal-free graphitic carbon nitride/black phosphorus photocatalyst synthesized via high-energy ball-milling for efficient hydrogen evolution and hexavalent chromium reduction, *J. Hazard. Mater.*, 2021, **413**, 2008247.

7 C. Fang, C. Xu, W. Zhang, M. Zhou, D. Tan, L. Qian, D. Hu, S. Jin and M. Zhu, Dual-quartet phosphorescent emission in the open-shell M_1Ag_{13} (M = Pt, Pd) nanoclusters, *Nat. Commun.*, 2024, **15**, 5962.

8 Y. Du, H. Sheng, D. Astruc and M. Zhu, Atomically Precise Noble Metal Nanoclusters as Efficient Catalysts: A Bridge between Structure and Properties, *Chem. Rev.*, 2020, **120**, 526–622.

9 Y. Wang, X.-H. Liu, R. Wang, B. Cula, Z.-N. Chen, Q. Chen, N. Koch and N. Pinna, Secondary Phosphine Oxide Functionalized Gold Clusters and Their Application in Photoelectrocatalytic Hydrogenation Reactions, *J. Am. Chem. Soc.*, 2021, **143**, 9595–9600.

10 H. Wang, X. Zhang, W. Zhang, M. Zhou and H.-L. Jiang, Heteroatom-Doped Ag_{25} Nanoclusters Encapsulated in Metal-Organic Frameworks for Photocatalytic Hydrogen Production, *Angew. Chem., Int. Ed.*, 2024, e202401443.

11 C. Wang, P. Lv, D. Xue, Y. Cai, X. Yan, L. Xu, J. Fang and Y. Yang, Zero-Dimensional/Two-Dimensional $Au_{25}(Cys)_{18}$ Nanoclusters/g-C_3N_4 Nanosheets Composites for Enhanced Photocatalytic Hydrogen Production under Visible Light, *ACS Sustain. Chem. Eng.*, 2018, **6**, 8447–8457.

12 Y. Negishi, M. Mizuno, M. Hirayama, M. Omatoi, T. Takayama, A. Iwasea and A. Kudo, Enhanced photocatalytic water splitting by $BaLa_4Ti_4O_{15}$ loaded with ~1 nm gold nanoclusters using glutathione-protected Au_{25} clusters, *Nanoscale*, 2013, **5**, 7188.

13 Y. Du, C. Li, Y. Dai, H. Yin and M. Zhu, Recent progress in atomically precise metal nanoclusters for photocatalytic application, *Nanoscale Horiz.*, 2024, **9**, 1262.

14 X. Lu, A. Tong, D. Luo, F. Jiang, J. Wei, Y. Huang, Z. Jiang, Z. Lu and Y. Ni, Confining single Pt atoms from Pt clusters on multi-armed CdS for enhanced photocatalytic hydrogen evolution, *J. Mater. Chem. A*, 2022, **10**, 4594.

15 Y. Wang, X.-H. Liu, Q. Wang, M. Quick, S. A. Kovalenko, Q.-Y. Chen, N. Koch and N. Pinna, Insights into Charge Transfer at an Atomically Precise Nanocluster/Semiconductor Interface, *Angew. Chem., Int. Ed.*, 2020, **59**, 7748–7754.

16 X. Huang, K. Yin, S. Zhang, T. Wu, Y. Yuan, X. Wang, Y. Jia, Z. Xiao, J. Gu and D. Wang, Interfacial chemical bond-modulated Z-scheme $Cs_2AgBiBr_6/WO_3$ enables stable and highly efficient photocatalysis, *Appl. Surf. Sci.*, 2023, **637**, 157877.

17 J. Wang, X. Li, Y. You, X. Yang, Y. Wang and Q. Li, Interfacial coupling induced direct Z-scheme water splitting in metal-free photocatalyst: C_3N/g-C_3N_4 heterojunctions, *Nanotechnology*, 2018, **29**, 365401.

18 Q. Zhu, H. Shen, C. Han, L. Huang, Y. Zhou, Y. Du, X. Kang and M. Zhu, Rationally construction of atomic-precise interfacial charge transfer channel and strong build-in electric field in nanocluster-based Z-scheme heterojunctions with enhanced photocatalytic hydrogen production, *Nano Res.*, 2024, **17**, 5002–5010.

19 Y. Du, J. Li, X. Ma and Q. Guo, Visible light driven mesoporous ag/Ag_2CrO_4/g-C_3N_4 degrades multiple organic pollutants efficiently: synthesis, mechanism, and degradation pathway, *Vacuum*, 2024, **226**, 113323.

20 S. O. Lee, S. K. Lakhera and K. Yong, Strategies to Enhance Interfacial Spatial Charge Separation for High-Efficiency Photocatalytic Overall Water-Splitting: A Review, *Adv. Energ. Sust. Res.*, 2003, **4**, 2300130.

21 S. Nematulloev, A. Sagadevan, B. Alamer, A. Shkurenko, R. Huang, J. Yin, C. Dong, P. Yuan, K. E. Yorov, A. A. Karluk, W. J. Mir, B. E. Hasanov, M. N. Hedhili, N. M. Halappa, M. Eddaoudi, O. F. Mohammed, M. Rueping and O. M. Bakr, Atomically Precise Defective Copper Nanocluster Catalysts for Highly Selective C-C Cross-Coupling Reactions, *Angew. Chem., Int. Ed.*, 2023, **62**, e202303572.

22 R. P. B. Silalahi, Y. Jo, J.-H. Liao, T.-H. Chiu, E. Park, W. Choi, H. Liang, S. Kahlal, J.-Y. Saillard, D. Lee and C. W. Liu, Hydride-containing 2-Electron Pd/Cu Superatoms as Catalysts for Efficient Electrochemical Hydrogen Evolution, *Angew. Chem., Int. Ed.*, 2023, **62**, e202301272.

23 D. Zhu and Q. Zhou, Nitrogen doped g-C_3N_4 with the extremely narrow band gap for excellent photocatalytic activities under visible light, *Appl. Catal., B*, 2021, **281**, 119474.

24 Z. Yu, Y. Li, A. Torres-Pinto, A. P. LaGrow, V. M. Diaconescu, L. Simonelli, M. J. Sampaio, O. Bondarchuk, I. Amorim, A. Araujo, A. M. T. Silva, C. G. Silva, J. L. Faria and L. Liu, Single-atom Ir and Ru anchored on graphitic carbon nitride for efficient and stable electrocatalytic/photocatalytic hydrogen evolution, *Appl. Catal., B*, 2022, **310**, 121318.

25 W. Sun, S. Jin, W. Du, X. Kang, A. Chen, S. Wang, H. Sheng and M. Zhu, Total Structure Determination of the $Pt_1Ag_9[P(Ph\text{-}F)_3]_7Cl_3$ Nanocluster, *Eur. J. Inorg. Chem.*, 2020, 590–594.

26 X. Lin, K. Sun, X. Fu, X. Ren, Y. Yang, C. Liu and J. Huang, Correlating Kernel−Shell Structures with Optical Properties of Pt_1Ag_{24} and Pt_1Ag_{14} Nanoclusters, *J. Phys. Chem. C*, 2021, **125**, 2194–2201.

27 A. K. Das, S. Mukherjee, S. S. R, A. S. Nair, S. Bhandary, D. Chopra, D. Sanyal, B. Pathak and S. Mandal, Defects Engineering on Ceria and C−C Coupling Reactions Using $[Au_{11}(PPh_3)_7I_3]$ Nanocluster: A Combined Experimental and Theoretical Study, *ACS Nano*, 2020, **14**, 16681–16688.

28 P. Niu, L. Zhang, G. Liu and H.-M. Cheng, Graphene-Like Carbon Nitride Nanosheets for Improved Photocatalytic Activities, *Adv. Funct. Mater.*, 2012, **22**, 4763–4770.

29 W. Yan, L. Yan and C. Jing, Impact of doped metals on urea-derived g-C_3N_4 for photocatalytic degradation of antibiotics: structure, photoactivity and degradation mechanisms, *Appl. Catal., B*, 2019, **244**, 475–485.

30 X. Zhang, F. Wu, G. Li, L. Wang, J. Huang, A. Song, A. Meng and Z. Li, Mechanistic insight into the synergy between platinum cluster and indium particle dual cocatalysts for enhanced photocatalytic water splitting, *J. Colloid Interface Sci.*, 2024, **670**, 774–784.

31 C. Huang, Y. Wen, J. Ma, D. Dong, Y. Shen, S. Liu, H. Ma and Y. Zhang, Unraveling fundamental active units in carbon nitride for photocatalytic oxidation reactions, *Nat. Commun.*, 2021, **12**, 320.

32 X. Zhang, F. Wu, G. Li, L. Wang, J. Huang, A. Song, A. Meng and Z. Li, Construction of intramolecular donor-acceptor type carbon nitride for photocatalytic hydrogen production, *J. Colloid Interface Sci.*, 2024, **655**, 439–450.

33 A. Ma, Y. Ren, Y. Zuo, J. Wang, S. Huang, X. Ma and S. Wang, Ligand-controlled exposure of active sites on the Pd_1Ag_{14} nanocluster surface to boost electrocatalytic CO_2 reduction, *Chem. Commun.*, 2024, **60**, 3162–3165.

34 M. Xu, D. Li, K. Sun, L. Jiao, C. Xie, C. Ding and H.-L. Jiang, Interfacial Microenvironment Modulation Boosting Electron Transfer between Metal Nanoparticles and MOFs for Enhanced Photocatalysis, *Angew. Chem., Int. Ed.*, 2021, **60**, 16372–16376.

35 M. Xu, X. Ruan, D. Meng, G. Fang, D. Jiao, S. Zhao, Z. Liu, Z. Jiang, K. Ba, T. Xie, W. Zhang, J. Leng, S. Jin, S. K. Ravi and X. Cui, Modulation of Sulfur Vacancies in $ZnIn_2S_4$/MXene Schottky Heterojunction Photocatalyst Promotes Hydrogen Evolution, *Adv. Funct. Mater.*, 2024, **34**, 2402330.

36 X. Yang, Y. Zhang, J. Deng, X. Huo, Y. Wang and R. Jia, Fabrication of Porous Hydrophilic CN/PANI Heterojunction Film for High-Efficiency Photocatalytic H_2 Evolution, *Catalysts*, 2023, **13**(1), 139.

37 L. Mao, B. Zhai, J. Shi, X. Kang, B. Lu, Y. Liu, C. Cheng, H. Jin, E. Lichtfouse and L. Guo, Supercritical CH_3OH-Triggered Isotype Heterojunction and Groups in g-C_3N_4 for Enhanced Photocatalytic H_2 Evolution, *ACS Nano*, 2024, **18**, 13939–13949.

38 L. Wang, Y. Li, Y. Ai, E. Fan, F. Zhang, W. Zhang, G. Shao and P. Zhang, Tracking Heterogeneous Interface Charge Reverse Separation in $SrTiO_3$/NiO/NiS Nanofibers with In Situ Irradiation XPS, *Adv. Funct. Mater.*, 2023, **33**, 2306466.

39 F. Xing, C. Wang, S. Liu, S. Jin, H. Jin and J. Li, Interfacial Chemical Bond Engineering in a Direct Z-Scheme g-C_3N_4/MoS_2 Heterojunction, *ACS Appl. Mater. Interfaces*, 2023, **15**, 11731–11740.

40 H. Wang, Z. Chen, Y. Shang, C. Lv, X. Zhang, F. Li, Q. Huang, X. Liu, W. Liu, L. Zhao, L. Ye, H. Xie and X. Jin, Boosting Carrier Separation on a BiOBr/$Bi_4O_5Br_2$ Direct Z-Scheme Heterojunction for Superior Photocatalytic Nitrogen Fixation, *ACS Catal.*, 2024, **14**, 5779–5787.

41 H. Shi, C. Li, L. Wang, W. Wang, J. Bian and X. Meng, Photocatalytic reduction of nitrate pollutants by novel Z-scheme ZnSe/$BiVO_4$ heterostructures with high N_2 selectivity, *Sep. Purif. Technol.*, 2022, **300**, 121854.

42 G. Kresse and J. Hafner, Ab initio molecular dynamics for liquid metals, *Phys. Rev. B:Condens. Matter Mater. Phys.*, 1993, **47**, 558–561.

43 G. Kresse and J. Furthmuller, Efficient iterative schemes for ab initio total-energy calculations using a plane-wave basis set, *Phys. Rev. B:Condens. Matter Mater. Phys.*, 1996, **54**, 11169–11186.

44 W. Tang, E. Sanville and G. Henkelman, A grid-based Bader analysis algorithm without lattice bias, *J. Phys. Condens. Matter*, 2009, **21**, 084204.

45 L. Xu, M. Yang, S. J. Wang and Y. P. Feng, Electronic and optical properties of the monolayer group-IV monochalcogenides M X (M = Ge, Sn; X = S, Se, Te), *Phys. Rev. B*, 2017, **95**, 235434.

46 S. Grimme, J. Antony, S. Ehrlich and H. Krieg, A consistent and accurate ab initio parametrization of density functional dispersion correction (DFT-D) for the 94 elements H-Pu, *J. Chem. Phys.*, 2010, **132**, 154104.

47 X. Jia, J. Wang, Y. Lu, J. Sun, Y. Li, Y. Wang and J. Zhang, Designing SnS/MoS_2 van der Waals heterojunction for direct Z-scheme photocatalytic overall water-splitting by DFT investigation, *Phys. Chem. Chem. Phys.*, 2022, **24**, 21321–21330.